Quantifying multiple uncertainties in modelling shallow water-sediment flows: A stochastic Galerkin framework with Haar wavelet expansion and an operator-splitting approach

Ji Li[a, b], Zhixian Cao[a *], Alistair G. L. Borthwick[c, d]

[a] *State Key Laboratory of Water Resources and Hydropower Engineering Science, Wuhan University, Wuhan 430072, China*;

[b] *Zienkiewicz Centre for Computational Engineering, Faculty of Science and Engineering, Swansea University, Swansea SA1 8EN, UK*;

[c] *Institute for Infrastructure and Environment, The University of Edinburgh, Edinburgh EH9 3FG, UK*.

[d] *School of Engineering, Computing and Mathematics, University of Plymouth, Plymouth PL4 8AA, UK*.

*Corresponding authors: Zhixian Cao, e-mail: zxcao@whu.edu.cn

Highlights:

- A new stochastic model is proposed for quantifying multiple uncertainties in modelling shallow water-sediment flows
- A stochastic Galerkin framework with Haar wavelet expansion and an operator-splitting approach is used
- The model reproduces typical shallow water flow-sediment-bed evolutions with multiple uncertainties

Declaration of interest: none

Abstract

The interactive processes of shallow water flow, sediment transport, and morphological evolution constitute a hierarchy of multi-physical problems of significant interests in a spectrum of engineering and science areas. To date, modelling shallow water hydro-sediment-morphodynamic (SHSM) processes is subject to multiple sources of uncertainty arising from input data and incomplete understanding of the underlying physics. A stochastic SHSM model with multiple uncertainties has yet to be developed as most SHSM models still concern deterministic problems and only one has been recently extended to a stochastic setting, but is restricted to a single source of uncertainty. Here we first present a new probabilistic SHSM model incorporating multiple uncertainties within the stochastic Galerkin framework using a multidimensional tensor product of Haar wavelet expansion to capture local, nonlinear variations in joint probability distributions and an operator-splitting-based method to ensure the modelling system remain hyperbolic. Then, we verify the proposed model via benchmark probabilistic numerical tests with joint uncertainties introduced in initial and boundary conditions, matching established experiments of flow-sediment-bed evolutions driven by a sudden dam break and by a landslide dam failure and large-scale rapid flow-sediment-bed evolution in response to flash flood. The present work facilitates a promising modelling framework for quantifying multiple uncertainties in practical shallow water hydro-sediment-morphodynamic modelling applications.

Keywords: multiple joint uncertainties; shallow water hydro-sediment-morphodynamic model; Haar wavelets; operator-splitting; stochastic Galerkin method

1. Introduction

Shallow water-sediment flows play key roles in driving mass transport and morphological evolution on Earth. Over the last two decades, shallow water hydro-sediment-morphodynamic (SHSM) models and their variants have seen widespread applications in a series of physical and engineering problems involving interactive processes of shallow water flow, sediment transport and morphological evolution [1], including general fluvial sediment-laden flows [2-7] and geophysical mass flows such as debris flows, landslides, and turbidity currents [8-15]. In principle, SHSM model equations are constructed according to fundamental mass and momentum conservation laws, and include a system of nonlinear hyperbolic equations. Therefore, a set of SHSM model equations falls into the category of partial differential equations (PDEs). As is common with all PDEs, SHSM model equations inevitably contain a high level of uncertainty, due to our incomplete knowledge of the underlying physics and/or inevitable error in physical input parameters. For example, the modelling system can propagate multiple uncertainties arising from initial and boundary conditions, such as measurement errors in inflow discharge and topographical elevation, selection of friction coefficient like the Manning roughness parameter, choice of empirical parameters used in sediment transport estimation [16]. Although these uncertainties strongly affect the reliability of model predictions, their impacts are almost neglected by existing SHSM models that mainly concern deterministic problems. Therefore, to evaluate the impact of these uncertainties and subsequently to provide more reliable predictions for practical problems, it is therefore imperative to conduct studies of uncertainty quantification in SHSM equations with multiple sources of uncertainty, which however remain rare.

In the broad field of PDEs, uncertainty quantification methods mainly include statistic methods such as Monte-Carlo simulations and their variants, stochastic collocation and stochastic Galerkin methods. Monte-Carlo sampling often incurs excessively computational overheads because it usually requires thousands of deterministic model runs [17-19]. Comparatively, stochastic collocation and stochastic Galerkin methods offer good alternatives to statistic methods by substantially reducing or eliminating the need for repetitive sampling [20]. Both methods are able to capture the spatial-temporal evolution of probabilistic distributions of any physical variable, with each probabilistic distribution approximated by a proper basis expansion to represent random space. In general, polynomial chaos or generalized polynomial chaos (gPC) expansions are often selected as basis functions because they can represent the most common probabilistic distributions. Stochastic collocation method is a nonintrusive method, which repeatedly samples a deterministic model with different input values, and then use the numerical outputs to construct a stochastic solution based on certain interpolation and quadrature rules [21, 22]. The advantage of stochastic collocation is clear as it requires only repetitive executions of existing deterministic solvers. Unlike nonintrusive methods, stochastic Galerkin method involves a Galerkin projection in stochastic space to yield a series of deterministic equations, which are subsequently solved in a single model run to obtain the stochastic moments of the solution of the original uncertain problem. Consequently, the stochastic Galerkin method is relatively more difficult to implement, primarily due to the fact that the equations for the expansion coefficients are almost always coupled. Hence, new codes need to be developed to deal with such a larger and coupled system of equations. However, to achieve almost the same level of accuracy, all the

existing collocation methods require solutions of much larger number of equations than those of Galerkin methods, especially for higher dimensional random spaces when multiple joint uncertainties are considered. Furthermore, the aliasing errors in stochastic collocation can be significant, especially, again, for higher dimensional random spaces [23]. Overall, these observations collectively demonstrate that the stochastic Galerkin method is attractive, offering the most accurate solutions using the relatively a smaller number of equations in multi-dimensional random spaces.

Existing SG methods along with gPC have been widely used in many physical and engineering problems, such as diffusion [24], gas dynamics [25, 26], disperse two-phase flow [27], shallow water hydrodynamics [28, 29], and shallow water-sediment flows [16], where spectral convergence was obtained when the underlying solution was sufficiently smooth. However, when applied to nonlinear hyperbolic systems of conservation laws with multiple joint uncertainties, such as shallow water hydrodynamic models and SHSM models, the gPC-SG approach faces a major challenge of handling discontinuities in multi-dimensiona l random spaces [30]. Taking the SHSM models as an example, to achieve well-balanced property, preserve depth positivity at wet-dry fronts and integrate stable friction term, robustness measures that typically involve local and nonlinear operations on topography and flow variables [4] are necessarily required. However, these measures inevitably introduce additional stochastic discretisation errors and give rise to local and nonlinear variations in probability distributions [30, 31], which are poorly represented by the conventional gPC basis functions. Therefore, spurious undershoots in a polynomial approximation can result in negative water depths that will cause the model to crash [30]. The shortcomings of gPC basis

functions have inspired the development of alternative approaches to capture local, nonlinear variations in any probability distribution. Le Maître et al. [32] first used Haar wavelets, which are multiscale, recursively nested and overlapping basis functions, to provide a localised, piecewise-constant decomposition of any probability distribution. This approach was later generalized using multiwavelets to provide a piecewise-polynomial representation [33]. Wavelet basis functions and their variants have been successfully applied to intrusive models of the Euler equations [34], the Buckley-Leverett equation for groundwater flow [35], and the shallow water hydrodynamic equations [30]. Another challenge of applying gPC-SG approximation to nonlinear hyperbolic systems is loss of hyperbolicity. This phenomenon occurs because the resulting system of expansion coefficients is not necessarily hyperbolic as its Jacobian matrices may generate complex eigenvalues. Recently, to ensure the system remain well-behaved, an operator-splitting-based method is proposed for the Euler equations for gas dynamics [36], and a well-balanced version developed for the shallow water hydrodynamic equations without bed friction [37] and then extended for the SHSM model [16]. The main idea behind this method is to split the underlying hyperbolic system into a linear hyperbolic system and linear or nonlinear scalar equations with variable coefficients and source terms, for which the gPC-SG method obtains hyperbolic discretization. With the gPC-SG method applied to each of the subproblems, the resulting system of the equations for expansion coefficients is guaranteed hyperbolic. However, these aforementioned operator-splitting-based stochastic models were limited to a single source of uncertainty.

By taking advantage of the Haar wavelet basis function and an operator-splitting-based method, we present a new stochastic Galerkin model of the one-dimensional (1D) SHSM

equations with multiple joint uncertainties. Specifically, we extend the recent operator-splitting-based stochastic Galerkin SHSM model proposed by Li et al. [16] from a single source of uncertainty to multiple sources of uncertainty, using the Haar wavelet basis function to replace the gPC basis function. Probabilistic laboratory-scale tests with multiple sources of uncertainty are designed to verify the resulting stochastic model for flow-sediment-bed evolution driven by a sudden dam break [38] and by a landslide dam failure [39]. A probabilistic large-scale test is also conducted, devised to match the rapid flow-sediment-bed evolution in response to flash flood, which was observed in an ephemeral river Nahal Yatir, Israel [40].

2. Representation of uncertainty

2.1. Parameterisation of uncertain inputs

An important step before conducting numerical simulations of stochastic systems, regardless the form of numerical methods, is to properly identify the random variables so that the input uncertainty is accurately modelled. In terms of shallow water-sediment flows, the input uncertainties usually include initial and boundary conditions, such as measurement errors in topography and inflow discharge, choice of friction coefficient, selection of empirical parameters used in sediment transport estimation. To quantify these uncertainties, each input is parameterized by a finite number of independent random variables. Given D

$\xi_d \in [-1,1]$, forming a D- dimensional uncertainty space, i.e.,

$\boldsymbol{\xi} = (\xi_1, \ldots, \xi_D) \in \mathbb{R}^D$. This uncertainty space is introduced into any physical variable $A(x,t,\boldsymbol{\xi})$, which can be expanded as follows

$$A(x,t,\boldsymbol{\xi}) = \sum_{|\mathbf{k}|=0}^{K} \hat{A}_{\mathbf{k}}(x,t)\Phi_{\mathbf{k}}(\boldsymbol{\xi}) \tag{2.1}$$

where $\mathbf{k} = (k_1, \ldots, k_D)$ is a multi-index with $|\mathbf{k}| = k_1 + \ldots + k_D$, and k_d is the index of the univariate basis function $\Phi_{k_d}(\xi_d)$ in the ξ_d uncertainty dimension for $1 \le d \le D$. $\left\{\hat{A}_{\mathbf{k}}\right\}$, the set of stochastic modes, and $\left\{\Phi_{\mathbf{k}}(\boldsymbol{\xi})\right\}$ indicates a set of basis functions spanning the D-dimensional uncertainty space $\boldsymbol{\xi}$.

2.2. Haar wavelet expansion

In general, any basis function can be used to span the uncertainty space. However, under multiple uncertainties, robustness and stability cannot be guaranteed with a global polynomial basis, as demonstrated in Shaw et al. [30]. In this study, multidimensional Haar wavelet basis functions are selected to provide a localised, piecewise-constant decomposition spanning the space of multiple uncertainty dimensions. Haar wavelet basis functions have already been adopted for hyperbolic conservation laws without source terms [32, 34] and hydrodynamic models with friction [30], in favour of their reliable capture of probability distributions functions with discontinuities. Such distributions arise at points where the flow is highly nonlinear [30, 31], and are particularly expected at uncertain wet-dry fronts where there is a high probability of zero depth and low probabilities of positive depths. The construction of the Haar wavelet basis functions is first presented for a single uncertainty dimension, and then extended into multiple uncertainty dimensions.

Haar wavelets are multiscale, recursively nested and overlapping basis functions that are constructed by recursive, two-way subdivision of the uncertainty space, up to a maximum refinement level L determined by the user. For a single source of uncertainty (i.e., $D = 1$) and assuming a maximum refinement level L, the one-dimensional uncertainty space is spanned by 2^L basis functions that are organised recursively into a tree structure. A probability distribution defined on the uncertainty space can be represented by assembling all basis functions to form a piecewise-constant approximation composed of all the locally-constant stochastic elements. At the root of tree is the so-called father function $\phi(\xi)$

$$\phi(\xi) = \begin{cases} 1 & \text{if } -1 < \xi < 1 \\ 0 & \text{otherwise} \end{cases} \tag{2.2}$$

At each refinement level $m = 0,\ldots,L-1$, a series of Haar wavelet basis functions $\psi_j^{(m)}(\xi)$ is defined, where j is the position of the wavelet in the uncertainty space at refinement level m. The Haar wavelet basis functions $\psi_j^{(m)}(\xi)$ are defined as

$$\psi_j^{(m)}(\xi) = 2^{m/2}\psi(2^m(\xi+1) - 2j - 1) \tag{2.3}$$

where $m \in 0,\ldots,L-1$ and $j \in 0,\ldots,2^m - 1$. Eq. (2.3) is a translation and dilation of the so-called mother function $\psi(\xi)$, which is given by

$$\psi(\xi) = \begin{cases} 1 & \text{if } -1 < \xi < 0 \\ -1 & \text{if } 0 \le \xi < 1 \\ 0 & \text{otherwise} \end{cases} \tag{2.4}$$

The basis functions $\{\Phi_k(\xi)\}_{k\in\{0,\ldots,2^L-1\}}$ can be therefore defined by setting the father function $\phi(\xi)$ as the zeroth basis function $\Phi_0(\xi)$ and the Haar wavelet functions given by Eq. (2.3) as the subsequent basis functions with index $k > 0$,

$$\Phi_k(\xi)=\begin{cases}\phi(\xi) & \text{if } k=0\\ \psi_j^{(m)}(\xi) & \text{if } k>0\end{cases} \tag{2.5}$$

When the basis function index $k>0$, it can be determined through one-to-one mapping with a refinement level m and position j

$$k(m,j)=2^m+j \tag{2.6}$$

which can be inverted to determine m and j from k, i.e., $m=\text{Int}[\log_2(k)]$ and $j=k-2^m$. A set of univariate basis functions $\{\Phi_k(\xi)\}$ is an orthogonal system, i.e.,

$$\int \Phi_j(\xi)\Phi_l(\xi)d\xi=2\delta_{jl} \tag{2.7}$$

Here δ_{jl} is the Kronecker symbol. Equipped with these notations, any random variable can be expressed as

$$A(x,t,\boldsymbol{\xi})=\sum_{k=0}^{2^L-1}\hat{A}_k(x,t)\Phi_k(\boldsymbol{\xi}) \tag{2.8}$$

For multiple sources of uncertainty (i.e., $D>1$), the uncertainty dimensions can be spanned by a $D-$dimensional tensor product of the 1D basis functions with 2^{DL} stochastic modes, or by a $D-$dimensional truncated basis with a substantially reduced number of stochastic modes. To reduce the computational cost, basis truncation is commonly recommended for hyperbolic conservation laws without source terms [32, 41, 42]. However, it is demonstrated in Ref [30] that such truncation cannot preserve robustness when applied to probabilistic hydrodynamic model under multiple sources of uncertainty. Therefore, the tensor product basis is adopted in the present study. Accordingly, by taking a tensor product of the 1D Haar wavelet basis functions, the $D-$ dimensional tensor product basis is constructed as $\{\Phi_{\mathbf{k}}(\boldsymbol{\xi})\}_{\mathbf{k}\in\{0,\ldots,2^L-1\}^D}$, i.e.,

$$\left\{\Phi_{\mathbf{k}}(\boldsymbol{\xi})\right\}_{\mathbf{k}\in\{0,\ldots,2^L-1\}^D} = \prod \Phi_{k_1}(\xi_1),\ldots,\Phi_{k_D}(\xi_D) \tag{2.9}$$

It is easy to proof that a set of $D-$variate basis functions $\left\{\Phi_{\mathbf{k}}(\boldsymbol{\xi})\right\}_{\mathbf{k}\in\{0,\ldots,2^L-1\}^D}$ is also an orthogonal system, i.e.,

$$\int \Phi_{\mathbf{j}}(\boldsymbol{\xi})\Phi_{\mathbf{l}}(\boldsymbol{\xi})d\boldsymbol{\xi} = 2^D\delta_{\mathbf{jl}} \tag{2.10}$$

Therefore, $A(x,t,\boldsymbol{\xi})$ can be written as

$$A(x,t,\boldsymbol{\xi}) = \sum_{\mathbf{k}\in\{0,\ldots,2^L-1\}^D} \hat{A}_{\mathbf{k}}(x,t)\Phi_{\mathbf{k}}(\boldsymbol{\xi}) \tag{2.11}$$

In general, the tensor product basis can easily transfer the robustness measures from the deterministic context into the $D-$dimensional uncertainty space. Due to the locality of Haar wavelet functions, the uncertainty dimensions become decoupled from the physical dimensions. Therefore, it ensures that stochastic discretisation errors as governed solely by the choice of L, do not interfere with physical discretisation errors, which are solely determined by the deterministic formulation. Such decoupling means that nonlinear operations within the stochastic finite volume operators are calculated exactly over each locally constant stochastic element. It is also noted that under multiple sources of uncertainty, the number of basis functions required to span multidimensional random space can quickly grow, exponentially increasing computational and storage costs so that they spiral out of control – the so-called "curse-of-dimensionality" [20].

3. SHSM model with multiple sources of uncertainty

3.1. Deterministic SHSM model

Li et al. [16] recently proposes a well-balanced, operator-splitting-based model of one-dimensional (1D) shallow water hydro-sediment-morphodynamic equations, which can be expressed in a standard, well-structured conservative form as follows

$$\frac{\partial \mathbf{U}}{\partial t}+\frac{\partial \mathbf{F}^{\mathrm{I}}(\mathbf{U})}{\partial x}=0 \tag{3.1}$$

and

$$\frac{\partial \mathbf{U}}{\partial t}+\frac{\partial \mathbf{F}^{\mathrm{II}}(\mathbf{U})}{\partial x}=\mathbf{S}_b+\mathbf{S}_f \tag{3.2}$$

in which

$$\mathbf{U}=\begin{bmatrix}\eta\\ q\\ h_s\end{bmatrix}=\begin{bmatrix}\eta\\ hu\\ hc\end{bmatrix},\quad \mathbf{F}^{\mathrm{I}}=\begin{bmatrix}hu\\ a^2\eta\\ huc\end{bmatrix},\quad \mathbf{F}^{\mathrm{II}}=\begin{bmatrix}0\\ hu^2+0.5g(\eta^2-2\eta z_b)-a^2\eta\\ 0\end{bmatrix} \tag{3.3a, 3.3b, 3.3c}$$

$$\mathbf{S}_b=\begin{bmatrix}0\\ -g\eta\dfrac{\partial z_b}{\partial x}\\ 0\end{bmatrix},\quad \mathbf{S}_f=\begin{bmatrix}0\\ N(\mathbf{U})\\ E-D\end{bmatrix} \tag{3.3d, 3.3e}$$

$$N(\mathbf{U})=-\frac{\tau_b}{\rho}-\frac{(\rho_s-\rho_f)gh^2}{2\rho}\frac{\partial c}{\partial x}-\frac{(\rho_0-\rho)(E-D)u}{(1-p)\rho} \tag{3.3f}$$

and

$$\frac{\partial z_b}{\partial t}=-\frac{E-D}{1-p} \tag{3.4}$$

where $\mathbf{U}$ represents the vector of conservative dependent variables; $\mathbf{F}$

$\mathbf{S}_b$ $\mathbf{S}_f$

t is time, x is streamwise coordinate; g is gravitational acceleration; h is the depth of the water-sediment mixture,

z_b is the bed elevation above the fixed horizontal datum, $\eta = h + z_b$; u is the depth-averaged velocity of the water-sediment mixture in the streamwise ($x-$) direction; c is the depth-averaged volumetric sediment concentration; $q = hu$ is the discharge; $h_s = hc$ is the equivalent thickness of the sediment phase; $q_s = h_s u$ is the sediment discharge; ρ_f and ρ_s are the pure densities of the water and sediment phases; $\rho = \rho_s c + \rho_f (1-c)$ is the density of the water-sediment mixture; $\rho_0 = \rho_s (1-p) + \rho_f p$ is the density of the bed material; p is the bed sediment porosity, and thus $1-p$ is the volumetric sediment concentration of the stationary bed; τ_b is the bottom shear stress for the water-sediment mixture; and E and D are the size-specific sediment entrainment and deposition fluxes.

The first subsystem (3.1) is a linear hyperbolic system whose Jacobian has three distinct real eigenvalues $\lambda_{1,2} = \pm a$ and $\lambda_3 = u$, where the parameter $a > 0$ is chosen to satisfy the following sub-characteristic condition:

$$-a \le u - \sqrt{gh} \le u + \sqrt{gh} \le a \tag{3.5}$$

When the term $\mathbf{S}_f$ is not present on the right-hand side, the second system (3.2) is essentially a scalar Burgers equation for q with variable coefficient and bed gradient term, given that η and h_s remain constant in time in Eq. (3.2). Furthermore, the value of a is set larger than the characteristic speed related to the second equation of the second subsystem (3.2), such that

$$a = \sup\left\{\max(|u| + \sqrt{gh},\ 2|u|)\right\} \tag{3.6}$$

Under this sub-characteristic condition, it is straightforward to check that each subsystem is

strictly hyperbolic. Therefore, after applying the Haar wavelet approximation and stochastic Galerkin projection, each resulting subsystem remains hyperbolic.

Li et al. [16] has provided a detailed description of the model equations, the model closures and the numerical algorithm. Briefly, the model has been constructed according to continuum mechanics principles, and includes mass and momentum conservation equations for the water-sediment mixture and separate mass conservation equations for sediment and bed material. To close the governing equations, relationships must be introduced to determine shear stresses and sediment exchange fluxes. The bottom shear stress is determined by the Manning resistance relationship. Estimation of sediment exchange with the bed is one of the key components of computational models of shallow water-sediment flows. Here, we follow the conventional practice in fluvial hydraulics [1] to estimate the sediment exchange with the bed. In short, two distinct primary mechanisms promote sediment exchange between the flow and the bed: bed sediment entrainment due to turbulence and sediment deposition by gravitational action. Although all the empirical relationships presented above are not new at all in the general field of shallow water hydro-sediment-morphodynamics, empiricism and uncertainty are inevitably introduced due to the incomplete understanding of the underlying physics. The model closures are described in detail Text S1 in Supplementary materials. The governing equations are numerically solved using an adapted version of a well-balanced numerical algorithm presented in Qian et al. [4]. Briefly, as bed deformation is entirely determined by local entrainment and deposition fluxes under the non-capacity framework for sediment transport, Eq. (3.4) is separated from the remaining equations and can be readily solved. Within the framework of Slope LImiter Centred (SLIC) scheme [43], a surface

$\mathbf{U}_i$ and bed elevation $z_{b,i}$ at a spatial node i and a time level n are presented as piecewise-constant fields over a uniform 1D mesh with spatial step of Δx.

To verify the operator-splitting approach, we first undertake a deterministic numerical test concerning a dam break flow over a fixed bed, which is numerically designed by Chertock et al. [37]. The computational domain is [-1 m, 1 m], and the bed profile includes a hump centred at $x =$ 0 m, which is defined as

$$z_b(x) = \begin{cases} 0.125(\cos(5\pi x)+1)+0.1 & -0.2 \le x \le 0.2 \\ 0.1 & \text{otherwise} \end{cases} \tag{3.7}$$

Following Chertock et al. [37], the gravitational constant $g =$ 1 and the initial water surface is set as

$$\eta(x)_{t=0} = \begin{cases} 1.0 & x \le 0.0 \\ 0.5 & x > 0.0 \end{cases} \tag{3.8}$$

At the upstream ($x =$ -1 m) and downstream ($x =$ 1 m) boundaries, a non-reflecting transmissive condition [43] was imposed with the values of all the primitive variables at the outlet nodes set equal to those at internal nodes closest to the boundary. Fig. 1 displays the computed results of water surface (a) and discharge (b) at $t =$ 0.8 s using splitting and non-splitting methods, which show good agreements between the two numerical predictions. This test demonstrates that the operator-splitting approach results in a good shock capturing

scheme as compared with its non-splitting counterpart in the deterministic setting, enhancing the confidence for establishing the stochastic problem.

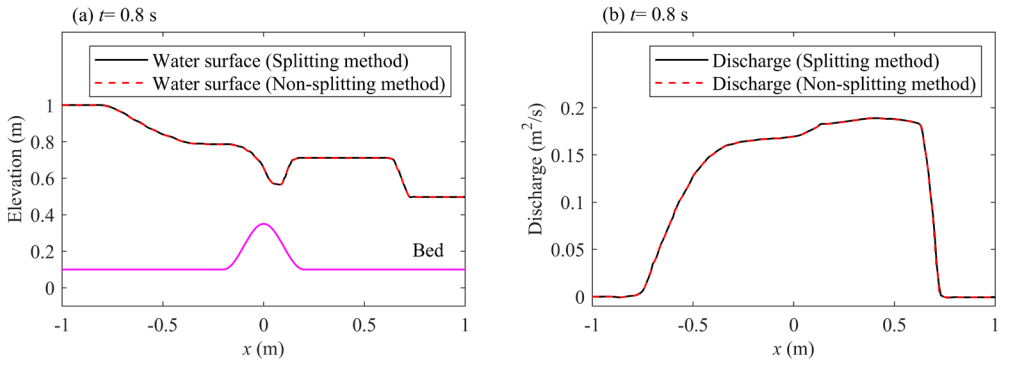

Fig.1. Idealized dam break over a fixed bed: model predictions of water surface and discharge at $t =$ 0.8 s using operator-splitting (solid lines) and non-splitting methods (dashed lines).

3.2. Stochastic Galerkin reformulation of the deterministic model

Next, we conduct the stochastic Galerkin reformulation of the governing equation system. Stochastic Galerkin reusing the Haar wavelet expansion, the vector of conserved variables in the nonlinear SHSM equations is approximated as follows

$$\mathbf{U}(x,t,\xi)=\sum_{\mathbf{k}\in\{0,\ldots,2^L-1\}^D}\hat{\mathbf{U}}_{\mathbf{k}}(x,t)\Phi_{\mathbf{k}}(\xi) \tag{3.9}$$

Substituting Eq. (3.9) into discretization of equation system Eq. (3.1) and Eq. (3.2) and bed deformation equation Eq. (3.4) and then conducting a stochastic Galerkin projection yields the following equations for the Haar wavelet expansion coefficients.

$$\hat{\mathbf{U}}^{*}_{i,\mathbf{k}}=\hat{\mathbf{U}}^{n}_{i,\mathbf{k}}-\frac{\Delta t}{\Delta x}\left[\left\langle\mathbf{F}^{\mathrm{I}}_{i+1/2}\Phi_{\mathbf{k}}(\xi)\right\rangle-\left\langle\mathbf{F}^{\mathrm{I}}_{i-1/2}\Phi_{\mathbf{k}}(\xi)\right\rangle\right] \tag{3.10}$$

$$\hat{\mathbf{U}}^{\dagger}_{i,\mathbf{k}}=\hat{\mathbf{U}}^{*}_{i,\mathbf{k}}-\frac{\Delta t}{\Delta x}\left[\left\langle\mathbf{F}^{\mathrm{II}}_{i+1/2}\Phi_{\mathbf{k}}(\xi)\right\rangle-\left\langle\mathbf{F}^{\mathrm{II}}_{i-1/2}\Phi_{\mathbf{k}}(\xi)\right\rangle\right]+\Delta t\left\langle\overline{\mathbf{S}}_{b,i}\Phi_{\mathbf{k}}(\xi)\right\rangle \tag{3.11a}$$

$$\hat{\mathbf{U}}_{i,\mathbf{k}}^{n+1} = \hat{\mathbf{U}}_{i,\mathbf{k}}^{\dagger} + \Delta t \left\langle \mathbf{S}_f^{RK} \Phi_{\mathbf{k}}(\boldsymbol{\xi}) \right\rangle \tag{3.11b}$$

$$\hat{z}_{b,i,\mathbf{k}}^{n+1} = \hat{z}_{b,i,\mathbf{k}}^{n} - \Delta t \left\langle \frac{(E-D)^{RK}}{1-p} \Phi_{\mathbf{k}}(\xi) \right\rangle \tag{3.12}$$

where $\langle \bullet \rangle$ is the so-called expectation operator, defined as the expected value over the uncertainty space; Δt is the time step; Δx is the spatial step; subscript i denotes the spatial node index; superscript n denotes the time step index; superscript * indicates the state after calculating the variables from Eq. (3.10), superscript † denotes the state after Eq. (3.11a); $\mathbf{F}_{i+1/2}^{\mathrm{I}or\,\mathrm{II}}$ and $\mathbf{F}_{i-1/2}^{\mathrm{I}or\,\mathrm{II}}$ represent the inter-cell numerical fluxes, and they are evaluated using the well-balanced SGM version of the finite volume SLIC scheme, which is also capable of preserving stochastic steady static state [16]. The bed slope source term $\overline{\mathbf{S}}_{bi}$ is discretized with a centered difference scheme [4], which is well-balanced with flux gradients. The source term $\mathbf{S}_f$ is determined using the second-order RK method, while the bed deformation is updated by the discretization of Eq. (3.12) with sediment exchange estimated by the RK method. To solve the SHSM model with multiple uncertainties, an alternative method is to use stochastic collocation [22]: one can apply a deterministic scheme to each sample point in random space, solve them separately to obtain the solution ensemble, and then construct an approximation, e.g., a gPC approximation, to the stochastic solution in the random space. On the other hand, the stochastic Galerkin method is able to provide better accuracy per stochastic degree of freedom, and with suitably designed solver, is quite competitive with collocation and the costs can be lower for high dimensional random inputs.

As Haar wavelet basis functions are used, the expectation operator can be calculated by a compatible Haar wavelet quadrature rule. The 2^{DL} quadrature points $\boldsymbol{\xi}_{\mathbf{p}}$ are positioned at the centres of the locally constant stochastic elements:

$$\boldsymbol{\xi}_{\mathbf{p}} = \frac{\Delta\boldsymbol{\xi}}{2} + \mathbf{p}\Delta\boldsymbol{\xi} - \{1\}^D, \quad \mathbf{p} \in \mathbf{P} \tag{3.13}$$

where $\Delta\boldsymbol{\xi} = \{2/2^L\}^D$, and $\mathbf{P} = \{0,\ldots,2^L\text{-}1\}^D$, which is the index set of stochastic elements. The quadrature weight $\omega = 2^D/2^{DL}$ is the size of a stochastic element, and the quadrature rule is defined as

$$\hat{A}_{\mathbf{k}} = \left\langle A(\boldsymbol{\xi})\Phi_{\mathbf{k}} \right\rangle = \frac{1}{2^D} \int_{[-1,1]^D} A(\boldsymbol{\xi})\Phi_{\mathbf{k}}(\boldsymbol{\xi})d\boldsymbol{\xi} \approx \frac{1}{2^D} \sum_{\mathbf{p}\in\mathbf{P}} \omega A(\boldsymbol{\xi}_{\mathbf{p}})\Phi_{\mathbf{k}}(\boldsymbol{\xi}_{\mathbf{p}}) \tag{3.14}$$

Eq. (3.14) can be universally used to evaluate the $\mathbf{k}$ th stochastic mode of any quantity $A(\boldsymbol{\xi})$. For example, the expectation of the numerical flux $\left\langle \mathbf{F}^{\mathrm{I}\,or\,\mathrm{II}}_{i+1/2}\Phi_{\mathbf{k}}(\boldsymbol{\xi}) \right\rangle$ appearing in Eq. (3.10) and Eq. (3.11) can be calculated using the Haar wavelet quadrature rule

$$\left\langle \mathbf{F}^{\mathrm{I}\,or\,\mathrm{II}}_{i+1/2}\Phi_{\mathbf{k}}(\boldsymbol{\xi}) \right\rangle \approx \frac{1}{2^D} \sum_{\mathbf{p}\in\mathbf{P}} \omega \mathbf{F}^{\mathrm{I}\,or\,\mathrm{II}}_{i+1/2}(\bar{\mathbf{U}}^L_{i+1/2}(\boldsymbol{\xi}_{\mathbf{p}}), \bar{\mathbf{U}}^R_{i+1/2}(\boldsymbol{\xi}_{\mathbf{p}}))\Phi_{\mathbf{k}}(\boldsymbol{\xi}_{\mathbf{p}}) \tag{3.15}$$

where $\bar{\mathbf{U}}^L_{i+1/2}$ and $\bar{\mathbf{U}}^R_{i+1/2}$ are the modified inter-cell variable vectors, which are designed to preserve well-balanced property. The resulting stochastic SHSM model automatically satisfies the well-balanced property as the expectations of the numerical fluxes and the bed source term are all evaluated by Haar wavelet quadrature rule.

4. Numerical Tests

Three probabilistic numerical tests are conducted to verify the present stochastic SHSM

model under multiple joint uncertainties. The first two are designed to match established laboratory-scale experiments concerning flow-sediment-bed evolutions driven by a sudden dam break (Test 1) [38] and a landslide dam failure (Test 2) [39]. Indeed, these two experiments have been previously devised to verify the predecessor of the present model [16], which was limited to a single source of uncertainty. The last test is a large-scale one concerning the rapid and intense flow-sediment-bed evolution due to flash flood, which was observed in ephemeral river Nahal Yatir, Israel (Test 3) [40].

A fixed uniform mesh is adopted, and the spatial step is sufficiently fine to ensure mesh independence of the solution, i.e., essentially equivalent solutions are obtained with an even finer mesh. The spatial step Δx is set to be 0.01 m for Tests 1 and 2, while it is 1 m for Test 3. The Courant number Cr is 0.4. Bed porosity $p = 0.4$ is adopted for all the tests. It is assumed any random variable ξ_d follows a uniform probability distribution. Furthermore, the mean solution $\mathbb{E}(\mathbf{U})$ is simply given by the zeroth-order coefficient $\hat{\mathbf{U}}_0$ and the standard deviation by $\sigma(\mathbf{U}) = \sqrt{\sum_{|\mathbf{k}|=1}^{K} \hat{\mathbf{U}}_{\mathbf{k}}^2 \left\langle \Phi_{\mathbf{k}}^2 \right\rangle}$. Also, any physical variable $\mathbf{U}$ can result in a total of 2^{DL} model realisations, each of which is calculated by Eq. (2.11) along with the corresponding quadrature point $\boldsymbol{\xi}_{\mathbf{p}}$ given by Eq. (3.13).

4.1. Test 1: Flow-sediment-bed evolution due to instant dam break

The first test concerns flow-sediment-bed evolution due to an abrupt and full dam break. In a glass-walled flume of dimensions 6 m length × 0.25 m width × 0.7 m height, a series of experiments were conducted [38]. During the experiments, the dam break was generated by

$h_0 = 35$ cm upstream of the dam,

and the bed was dry downstream of the dam. The bed material comprised PVC pellets of diameter 3.92 mm and the density 1580 kg/m^3. Numerical modelling was performed until the forward and backward propagating waves reached the downstream and upstream boundaries; thus, the boundary conditions were merely kept at the initial static state.

This test is brought into a probabilistic setting by specifying joint uncertainties in the Manning roughness parameter n and the modification coefficient ϕ for calculating sediment transport rate at capacity regime q_b [see Eq. 7(b) in Li et al. [16]]. As large uncertainties are associated with the Manning roughness parameter and the modification coefficient [16], both parameters are therefore assumed to have 50% uncertainty following Li et al. [16]. The Manning roughness parameter has a mean value of $n =$ 0.026 m$^{-1/3}$ s [44], and the mean value of modification ϕ is calibrated to be 3.0 [3], respectively leading to $n(\xi_1) = 0.026 + 0.013\xi_1$ (m$^{-1/3}$ s), and $\phi(\xi_2) = 3.0 + 1.5\xi_2$.

This test example is first employed to examine the convergence of the proposed stochastic model under different refinement level L. With respect to the dam-break flow over an erodible bed, high-order convergence rate is not expected due to the existence of shock waves and wet-dry interfaces. To quantify the error of the predicted mean solution as compared with measured data, the non-dimensional discrepancy is defined based on the L^1-norm

$$L^1(f) = \frac{\sum_{i=1}^{N} abs(\overline{f}_i - \widehat{f}_i)}{\sum_{i=1}^{N} \overline{f}_i} \tag{4.1}$$

where the symbol f represents a physical variable such as water surface elevation and bed deformation thickness; N is the number of measured data; $\overline{f}$ denotes the predicted mean solution, whereas $\widehat{f}$ represents the measured data. The obtained results are listed in Table 1 along with their corresponding convergence rates. It reveals that increasing the refinement level results in a decay of L^1- norm values for the mean water surface elevation η and the mean bed deformation thickness Δz_b. As can be seen from the convergence rates presented in Table 1, when the refinement level $L \geq 3$, the convergence rate is around 1, indicating that a first-order accuracy is achieved in terms of the considered error norms. Henceforth, the present stochastic model is configured with refinement level $L = 3$. Indeed, this is also the minimum levels of refinement per uncertainty dimension to reliably capture complex probability distributions as required by the Haar wavelet basis function [30].

Table 1 L^1 norms and convergence rates of model predictions for Test 1 using different refinement level

Refinement Level	$L^1(\eta)$ -norm	Convergence rate	$L^1(\Delta z_b)$ -norm	Convergence rate
	$t = 0.25$ s			
1	1.03×10^{-1}	–	1.05×10^{-1}	–
2	6.26×10^{-2}	0.71	6.24×10^{-2}	0.75
3	2.65×10^{-2}	0.89	2.76×10^{-2}	0.91
4	1.32×10^{-2}	0.96	1.33×10^{-2}	0.94
5	6.12×10^{-3}	0.98	6.25×10^{-3}	1.01
	$t = 0.5$ s			
1	1.15×10^{-1}	–	9.82×10^{-2}	–
2	6.93×10^{-2}	0.72	5.89×10^{-2}	0.74
3	2.82×10^{-2}	0.91	2.72×10^{-2}	0.93
4	1.29×10^{-2}	0.95	1.26×10^{-2}	0.94
5	5.96×10^{-3}	1.01	5.46×10^{-3}	1.02
	$t = 1.5$ s			
1	1.12×10^{-1}	–	9.87×10^{-2}	–
2	6.03×10^{-2}	0.89	5.47×10^{-2}	0.85
3	2.97×10^{-2}	0.95	2.73×10^{-2}	0.93
4	1.36×10^{-2}	1.01	1.28×10^{-2}	0.98
5	6.23×10^{-3}	1.02	5.75×10^{-3}	1.03

With two uncertainty dimensions ($D = 2$) and refinement level $L = 3$, the present model results in 8×8= 64 stochastic modes and a probabilistic solution with 64 model realisations. Fig. 2 shows the probabilistic predictions of water surface and bed profiles under joint uncertainties in the Manning's roughness parameter $n(\xi_1)$ and modification coefficient $\phi(\xi_2)$, along with corresponding measurements obtained from Spinewine [38]. As can be seen from Fig. 2, the measured data of both water surfaces and bed elevations almost lie within the range of the probabilistic predictions. By contrast, when the model is limited to a single source of uncertainty, some discrepancies can be identified between measured and

predicted water level profiles irrespective of which uncertainty is considered [16]. In light of this point, the present model that incorporates multiple uncertainties is superior to its predecessor that is restricted to a single source of uncertainty. As shown in Fig. 2, the dam-break wave propagation speed as represented by water surface profiles is mainly affected by the Manning's roughness parameter, whilst the bed deformation is jointly affected by the Manning roughness parameter and the modification coefficient. This finding is consistent with that from Li et al. [16].

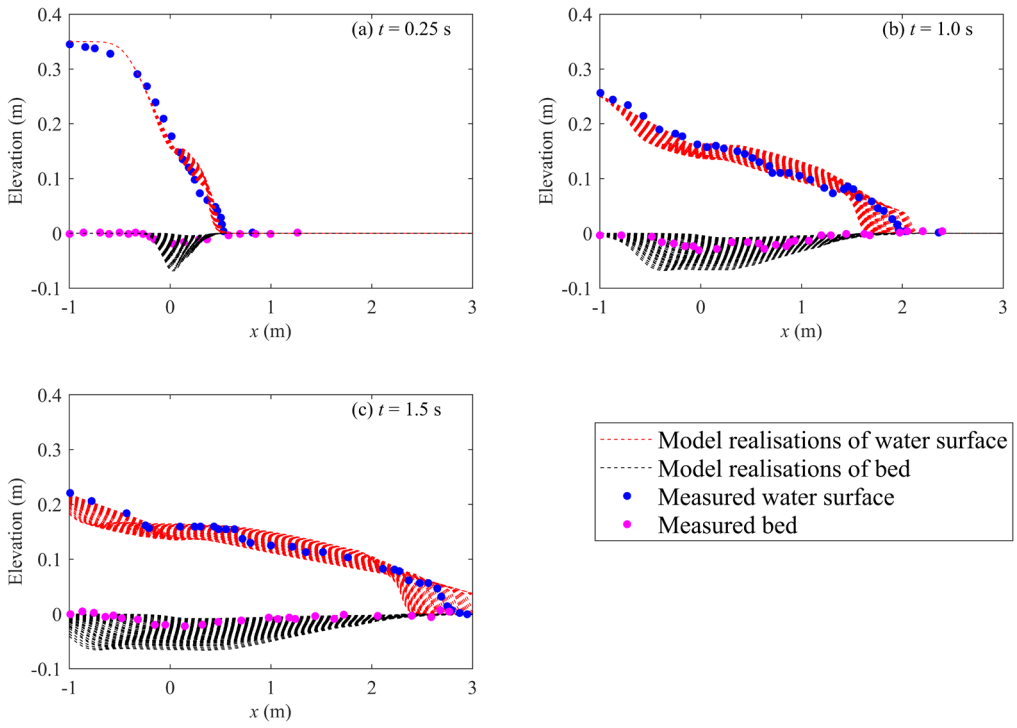

Fig. 2. Sudden dam break over an erodible bed: measurements (solid circles) from Spinewine [38] and probabilistic predictions of water surface and bed profiles (dashed lines) obtained for joint random Manning roughness parameter $n(\xi_1)$ and modification coefficient $\phi(\xi_2)$.

Fig. 3 shows the spatial-temporal evolution of the standard deviations of water surface, bed elevation, flow velocity, and sediment concentration for joint random Manning's roughness parameter $n(\xi_1)$ and modification coefficient $\phi(\xi_2)$. Table 2 summarizes the maximum values of the standard deviations of these physical variables. Correspondingly, their counterparts under a specific single source of uncertainty are also included. As seen from Table 2, all the physical variables under multiple uncertainties exhibit larger maximum values of standard deviations than those under a single uncertainty. Furthermore, by comparing Fig. 3 to the Fig. 4 in Li et al. [16], the standard deviations of the water surface $\sigma(\eta)$ and sediment concentration $\sigma(c)$ under multiple uncertainties are found to exhibit different behaviours from those under a single uncertainty. Specifically, under the joint effect of random $n(\xi_1)$ and $\phi(\xi_2)$, $\sigma(\eta)$ presents a major peak near the front of dam-break wave, unlike its counterpart under a single uncertainty that peaks close to the 'dam' site and then gradually decreases in the stream-wise direction. Moreover, $\sigma(c)$ under joint uncertainties develops a multi-peaked structure with one major peak placed approximately at the centre of the wave and several minor peaks located along the stream-wise direction. By contrast, $\sigma(c)$ under a single uncertainty presents a double-peaked behaviour with one peak located at the wave front and the other approximately at the centre of wave.

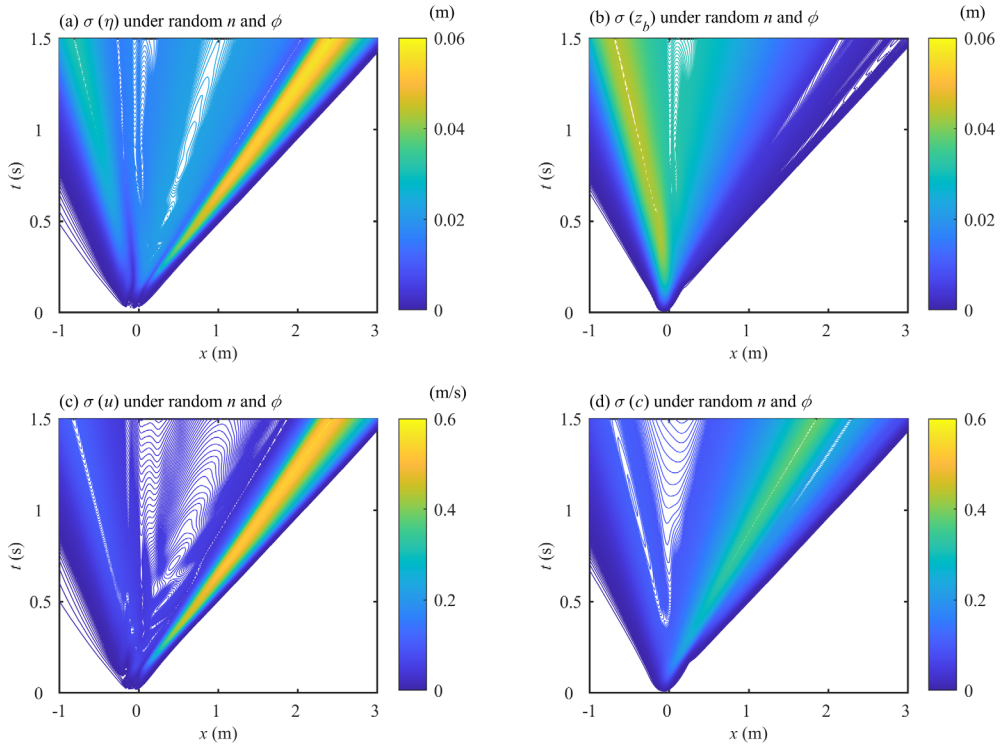

Fig. 3. Sudden dam-break: spatial-temporal evolutions of standard deviations of (a) water surface, (b) bed elevation, (c) flow velocity, and (d) sediment concentration for joint random Manning's roughness parameter $n(\xi_1)$ and modification coefficient $\phi(\xi_2)$.

Table 2 Summary of maximum standard deviations of all the physical variables (Test 1)

Results	Multiple sources of uncertainty in $n(\xi_1)$ and $\phi(\xi_2)$	A single source of uncertainty [16]	
		$n(\xi)$	$\phi(\xi)$
$\sigma(\eta)$ (m)	0.059	0.023	0.010
$\sigma(z_b)$ (m)	0.046	0.041	0.014
$\sigma(u)$ (m/s)	0.547	0.462	0.108
$\sigma(c)$	0.409	0.289	0.083

4.2. Test 2: Flow-sediment-bed evolution due to landslide dam failure

Next, we re-explore flow-sediment-bed evolution due to landslide dam failure, with probabilistic predictions compared with measured data from one of a series of flume experiments [39]. The experiments were carried out in a flume with dimensions 80 m length × 1.2 m width × 0.8 m height. The flume was made of glass with a fixed bed slope of 0.001, and the Manning's bed roughness coefficient n was approximately 0.012 $m^{-1/3}$ s. The experimental setup is displayed in Fig. 4. Twelve automatic water-level probes measured the stage time histories at different locations along the centre line of the flume. Stations CS1 to CS5 are upstream of the dam, whereas stations CS 6 to CS 12 are downstream. In the experiments, with an inflow discharge released from the flume inlet, the water level upstream of the dam gradually increased, and once the flow overtopped the dam crest, the dam failure occurred through erosion. Subsequently, flow upstream of the dam quickly receded along with dam failure. By contrast, three stages were witnessed in downstream flow evolution: initial rising, subsequently gradual recession and final stabilization. Following Li et al. [16], the case we revisited here (i.e., F- Case 11 considered in Cao et al. [39]) concerns a landslide dam with no initial breach, which is composed of non-cohesive uniform sediment of median diameter 0.8 mm and specific gravity 1.65. The initial upstream and downstream slopes of the dam were 1/2 and 1/3, and the initial static water depths immediately upstream and downstream of the dam were 0.054 m and 0.048m. The mean value of inlet flow discharge was 0.042 m^3/s. Therefore, at the inlet boundary of numerical model, the water depth and velocity were determined by the method of characteristics as the flow discharge was specified. A 0.15 m-high weir was placed at the outlet of the flume and controlled the downstream water level to keep it remain at the initial depth. It was observed that a hydraulic drop

occurred downstream of the weir during the course of the experiment, so the flow upstream of the weir was not affected by the outflow. Hence, a non-reflecting transmissive condition [43] was imposed at the downstream boundary (80 m).

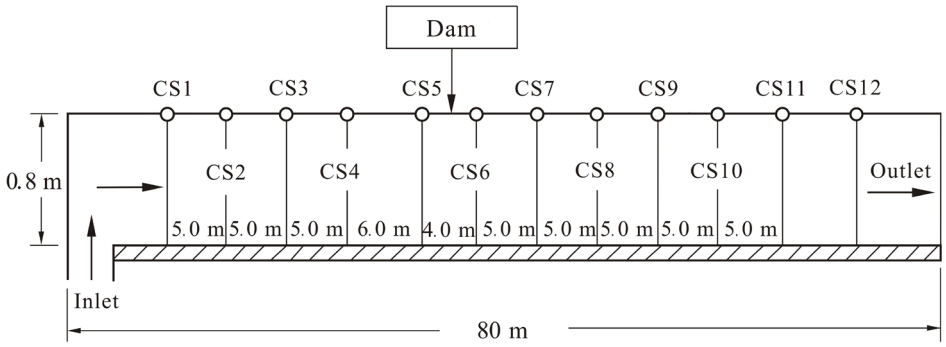

Fig. 4. Experimental setup for landslide dam failure [figure adapted from Cao et al. [39]].

Here, we investigate the impact of three joint uncertainties in the Manning's roughness parameter, the modification coefficient, and the inflow discharge, the last of which is also subject to a high level of uncertainty due to inevitable measurement error [45]. The steady inflow discharge is perturbed by 15% uncertainty, a suitable range for the modelling of fluvial flows [45]. Following Test 1, both the Manning roughness parameter and the modification coefficient are assumed to have 50% uncertainty. Therefore, $q_{in}(\xi_1) = 0.042 + 0.0063\xi_1$ (m^3/s), $n(\xi_2) = 0.012 + 0.006\xi_2$ ($m^{-1/3}s$), and $\phi(\xi_3) = 6.0 + 3.0\xi_3$. With three uncertainties ($D = 3$) and maximum refinement level $L = 3$, the model prediction therefore comprises 512 ($= 8 \times 8 \times 8$) stochastic modes and a solution of 512 model realisations.

Fig. 5 shows the probabilistic stage time histories predicted by the stochastic SHSM

$q_{in}(\xi_1)$, Manning roughness parameter $n(\xi_2)$, and modification coefficient $\phi(\xi_3)$. Corresponding measurements obtained by Cao et al. [39] at four selected locations along the channel are included for comparison. Stations CS 1, CS 5, CS 8 and CS 12 are located 19 m, 40 m, 54 m and 73.5 m downstream of the inlet (Fig. 3). As seen from Fig. 5, all the measured data have been fully bounded by the probabilistic predictions, showing the satisfactory performance of the proposed new model.

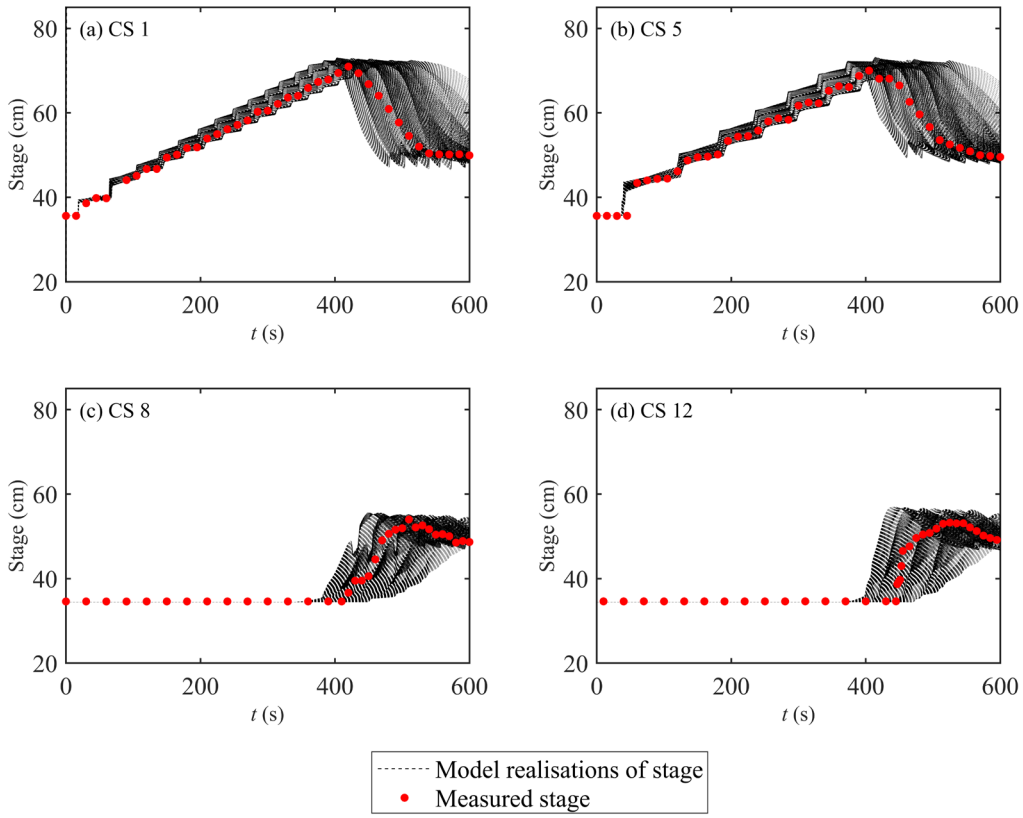

Fig. 5. Landslide dam failure: measurements (open circles) for F-Case 11 from Cao et al. [39] and probabilistic predictions (dashed lines) of stage time histories at 4 gauge points along the flume for three joint uncertainties in inflow discharge $q_{in}(\xi_1)$, Manning roughness parameter $n(\xi_2)$, and modification coefficient $\phi(\xi_3)$.

The probabilistic predictions of water surface and bed profiles under random inflow discharge, Manning roughness parameter and modification coefficient, along with measured data for water surface [39], are displayed in Fig. 6. At $t =$ 410 s (Fig. 6a), the water just overtops the dam and begins to erode the toe. The output uncertainty in the water surface upstream of the dam is relatively larger than its downstream counterpart. Meanwhile, the output uncertainty in the bed elevation exhibits a slight increase at the toe of dam. At $t =$ 430 s, the overtopping flow further erodes the downstream surface of the dam, with more erosion observed at $t =$ 450 s. The uncertainties in the water surface and bed elevation exhibit appreciable increase across the whole field. With time going on, the dam failure process gradually decreases. By $t =$ 600 s, the output uncertainty in the water surface downstream of the dam has decreased a lot, while its upstream counterpart still persists with a significant magnitude.

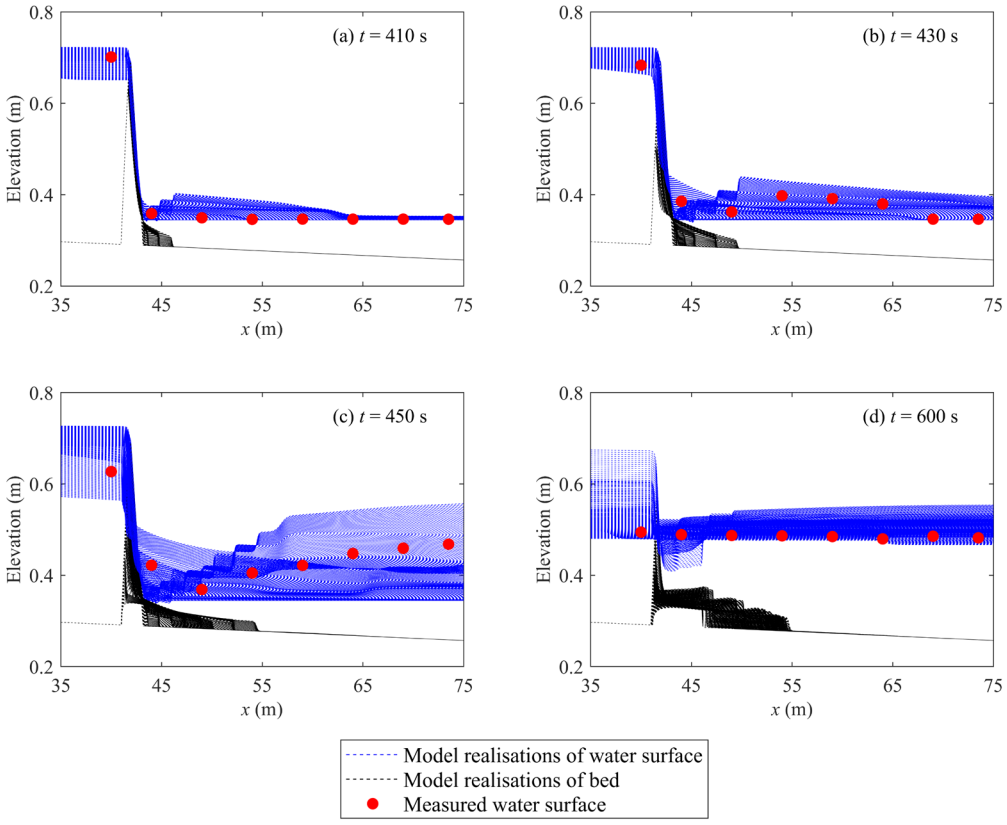

Fig. 6. Landslide dam failure: measured water surface (open circles) for F-Case 11 from Cao et al. [39] and probabilistic predictions of water surface, and bed profiles (dashed lines) along a channel for three joint uncertainties in inflow discharge $q_{in}(\xi_1)$, Manning roughness parameter $n(\xi_2)$, and modification coefficient $\phi(\xi_3)$.

Fig. 7 shows the spatial-temporal evolution of the standard deviations of water surface, bed elevation, flow velocity and sediment concentration under three joint uncertainties in inflow discharge $q_{in}(\xi_1)$ $n(\xi_2)$ $\phi(\xi_3)$

$\sigma(\eta)$ and flow velocity $\sigma(u)$ only increase upstream of the dam site due to the joint effect of random inflow discharge and Manning roughness parameter. Meanwhile, the standard deviations of the bed elevation $\sigma(z_b)$ and sediment concentration $\sigma(c)$ remain zero. After the water flows over the dam crest and triggers the dam breach, the standard deviations of all the physical variables accumulate rapidly with time and extend further toward the outlet. Subsequently, as the dam failure process decreases, the standard deviations exhibit a gradual shrink.

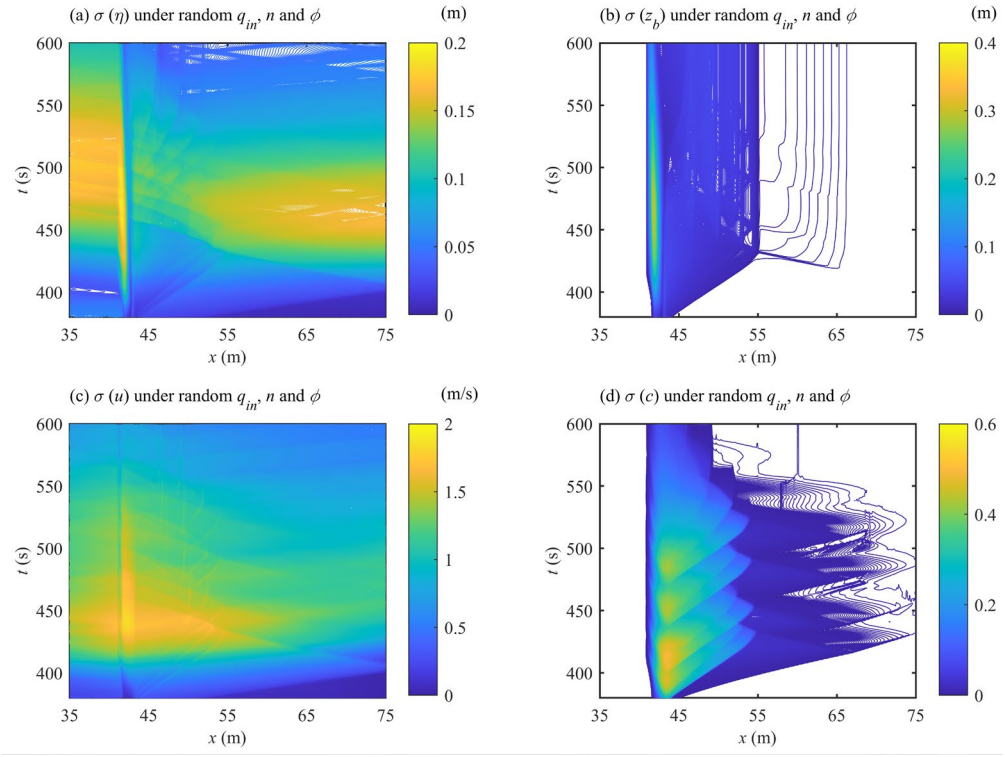

Fig. 7. Landslide dam failure: spatial-temporal evolutions of standard deviations of (a) water surface, (b) bed elevation, (c) flow velocity and (d) sediment concentration for three joint uncertainties in inflow discharge $q_{in}(\xi_1)$, Manning roughness parameter $n(\xi_2)$, and modification coefficient $\phi(\xi_3)$.

Table 3 Summary of maximum standard deviations of all the physical variables (Test 2)

Results	Multiple sources of uncertainty in $q_{in}(\xi_1)$, $n(\xi_2)$ and $\phi(\xi_3)$.	A single source of uncertainty [16]		
		$q_{in}(\xi)$	$n(\xi)$	$\phi(\xi)$
$\sigma(\eta)$ (m)	0.194	0.148	0.068	0.005
$\sigma(z_b)$ (m)	0.302	0.261	0.118	0.002
$\sigma(u)$ (m/s)	1.844	1.315	0.924	0.124
$\sigma(c)$	0.497	0.455	0.423	0.065

4.3. Test 3: Flow-sediment-bed evolution due to flash flood

Here, we examine a large-scale test concerning flow-sediment-bed evolution induced by flash flood [40], as opposed to the above laboratory-scale cases. In the 1990-1991 flood season, the rapid flow-sediment-bed evolutions in an ephemeral river Nahal Yatir in Israel were observed during five flash floods [40], with recorded maximum transport rate and unit flow discharge being respectively 7.05 kg/m/s and 1.43 m^2/s. The observation time varied from about 10 minutes to 90 minutes for each flood, which only covered part of the total duration of the hydrograph. In general, the typical total duration of a flash flood hydrograph, including both rising and recession phases, should range from some tens of minutes to a few hours. Given the limited information on these flash flood events [40], it is assumed that the flash flood hydrograph was triangular and symmetrical in shape, featuring a rising and recession phase of half an hour respectively. Also, the peak flow discharge q_p (= 1.5 m^2/s) was presumed to be a bit higher than the recorded maximum flow discharge (1.43 m^2/s), as field observation might miss the real peak flow discharge due to measurement error [46]. Moreover, an initial dry bed with a uniform slope of 0.009 is considered. The bed materials

comprised non-cohesive uniform sediment of median diameter 6 mm and specific gravity 1.65. The mean value of Manning's roughness parameter is 0.025 $m^{-1/3}s$. The computational reach is set to be long enough to ensure that the forward wave does not reach the downstream boundary within the time of computation, thus the downstream boundary condition is not needed. At the inlet boundary of numerical model, the water depth and velocity were determined by the method of characteristics as the inflow hydrograph was specified.

This large-scale test is extended into a probabilistic setting to investigate the flow-sediment-bed response to two joint uncertainties, which are associated with an error range for the inflow discharge and a range of choices for the Manning's roughness parameter. The unsteady inflow discharge $q_{in}(\xi_1)$ has a 15% uncertainty, so that $q_{in}(\xi_1) = 1.5 + 0.225\ \xi_1$ m^2/s. The Manning's roughness parameter is perturbed by 50% uncertainty, leading to $n(\xi_2) = 0.025 + 0.0125\,\xi_2$ $m^{-1/3}s$. Therefore, the probabilistic model is constructed with two uncertainty dimensions ($D = 2$) and maximum refinement level $L = 3$, resulting in 64 (= 8 × 8) stochastic modes and corresponding 64 model realisations.

Fig. 8 displays the probabilistic predictions of sediment transport rate against Shields parameter θ considering the joint effect of two uncertainties in inflow discharge and Manning's roughness parameter. Corresponding observed data are also included for comparison. As seen from Fig. 8, the computed transport rates fully bound all the measured data. Given the range of sediment transport rates of 10^{-1}~10 kg/m/s, the corresponding range of Shields parameter θ is about 10^{-1}~4×10^{-1}. In principle, this observation is rather consistent with the field data observed from Nahal Yatir [40].

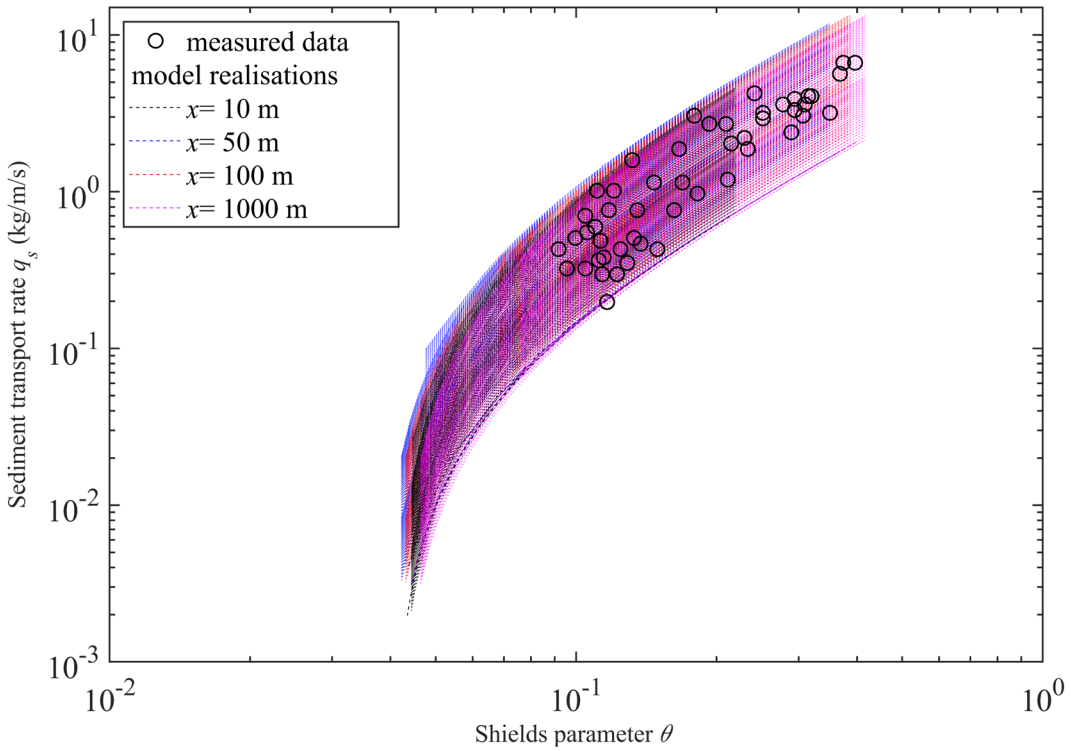

Fig. 8. Flash flood: measurements (open circles) and probabilistic predictions (dashed lines) of sediment transport rate against shields parameter at selected cross-sections for two joint uncertainties in inflow discharge $q_{in}(\xi_1)$ and Manning roughness parameter $n(\xi_2)$.

Fig. 9 shows the probabilistic flow discharge and sediment transport rate time histories at four cross-sections for joint uncertainties in inflow discharge and Manning's roughness parameter, and Fig. 10 presents the probabilistic predictions of stage and bed elevation time histories. In general, the peak flow discharges at the cross-sections exhibit appreciably higher values than those at the inlet boundary. This is mainly due to the contribution of the sediment obtained from the rapid bed scour near the inlet boundary, as shown in Fig. 10 (a and b). In particular, the bed scour near the inlet can reach as high as about 0.7 m within 60 mins at

$x =$

$x =$ 10 m (Fig. 9 b1) to about 22 kg/m/s at $x =$ 100 m (Fig. 9 b2). Furthermore, such a high sediment transport rate can be sustained for a rather long distance in the downstream direction (Figs. 9 b3 and b4). Also, flow with such a high sediment load only causes marginal erosion in the downstream (Figs. 10 c and d). When the inflow discharge gradually decreases to zero (i.e., $t >$ 30 min), the flow discharge, sediment transport rate and stage also reduce. Accordingly, the output uncertainties in the flow discharge, sediment transport and stage exhibit rapid increase along with the increase of inflow discharge and then gradually convert to zero as the inflow discharge reduces to zero. By contrast, the output uncertainty in the bed elevation only develops near the inlet boundary where rapid bed scour occurs. These finding are further confirmed by Fig. 11, where the spatial-temporal evolutions of standard deviations of water surface $\sigma(\eta)$, bed elevation $\sigma(z_b)$, flow velocity $\sigma(u)$ and sediment concentration $\sigma(c)$ are presented. Specifically, during the first rising phase of inflow hydrograph (i.e., $t <$ 30 min), the standard deviations of all these physical variables, except the bed elevation, increase rapidly with time and extend further downstream. By contrast, $\sigma(z_b)$ only accumulate in the area close to the inlet boundary. Subsequently, $\sigma(\eta)$, $\sigma(u)$ and $\sigma(c)$ experience a gradual shrink during the second recession phase of inflow hydrograph (i.e., $t >$ 30 min), whereas $\sigma(z_b)$ exhibit a slight increase near the inlet boundary and then remain almost unchanged as no further erosion occurs.

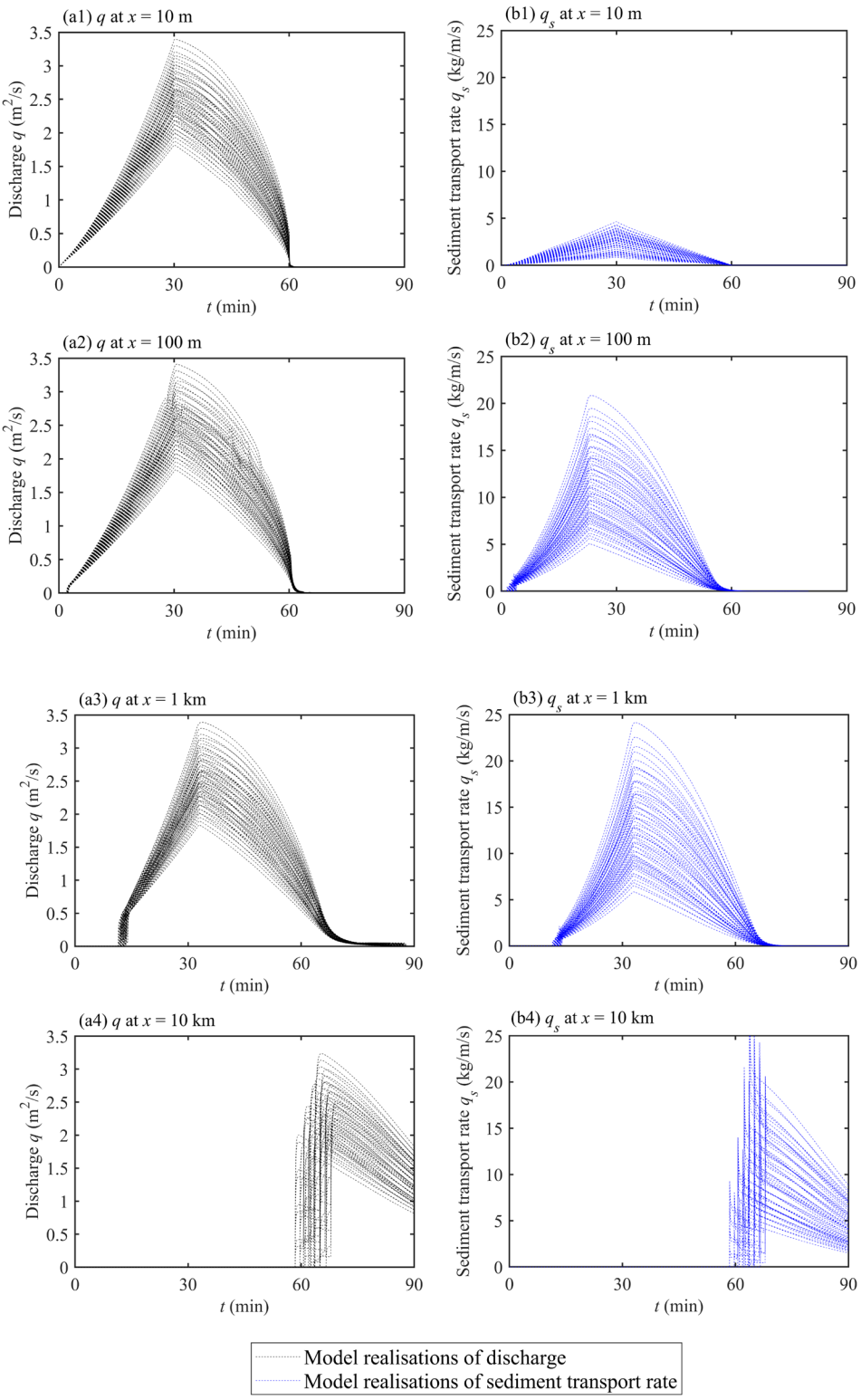

Fig. 9. Flash flood: probabilistic predictions of (a1-a4) discharge (black dashed lines) and (b1-b4) sediment transport rate (blue dashed lines) time histories at four cross-sections for two joint uncertainties in inflow discharge $q_{in}(\xi_1)$ and Manning roughness parameter $n(\xi_2)$.

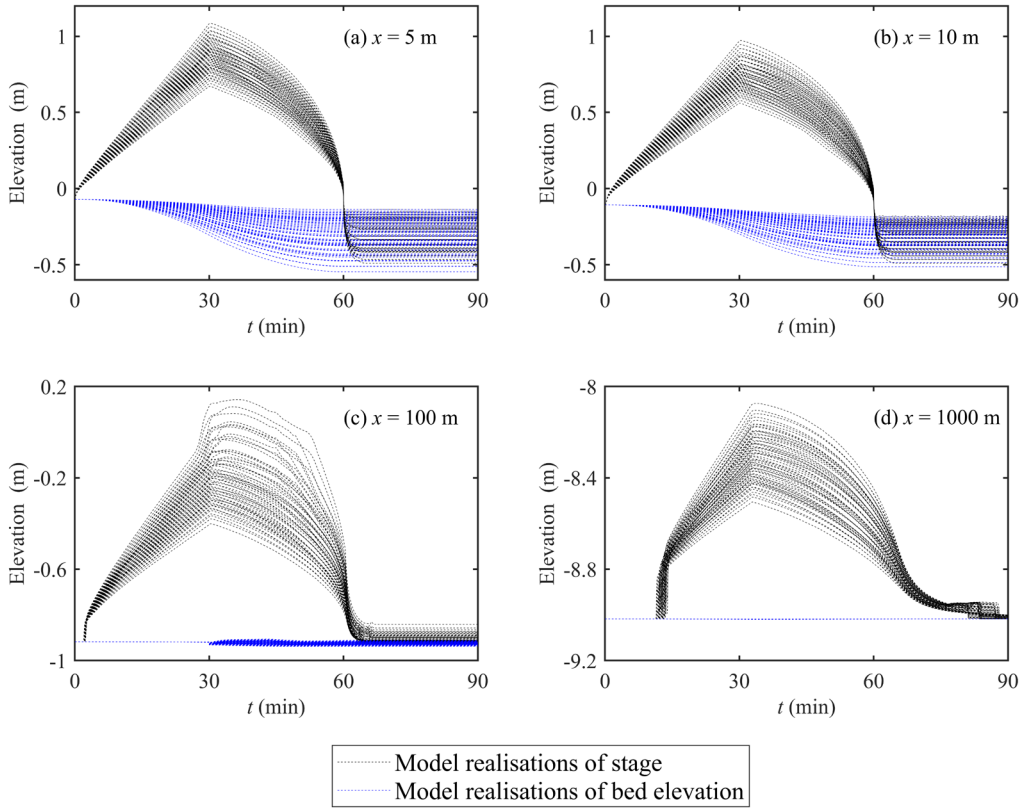

Fig. 10. Flash flood: probabilistic predictions of stage (black dashed lines) and bed elevation (blue dashed lines) time histories at four cross-sections for two joint uncertainties in inflow discharge $q_{in}(\xi_1)$ and Manning roughness parameter $n(\xi_2)$.

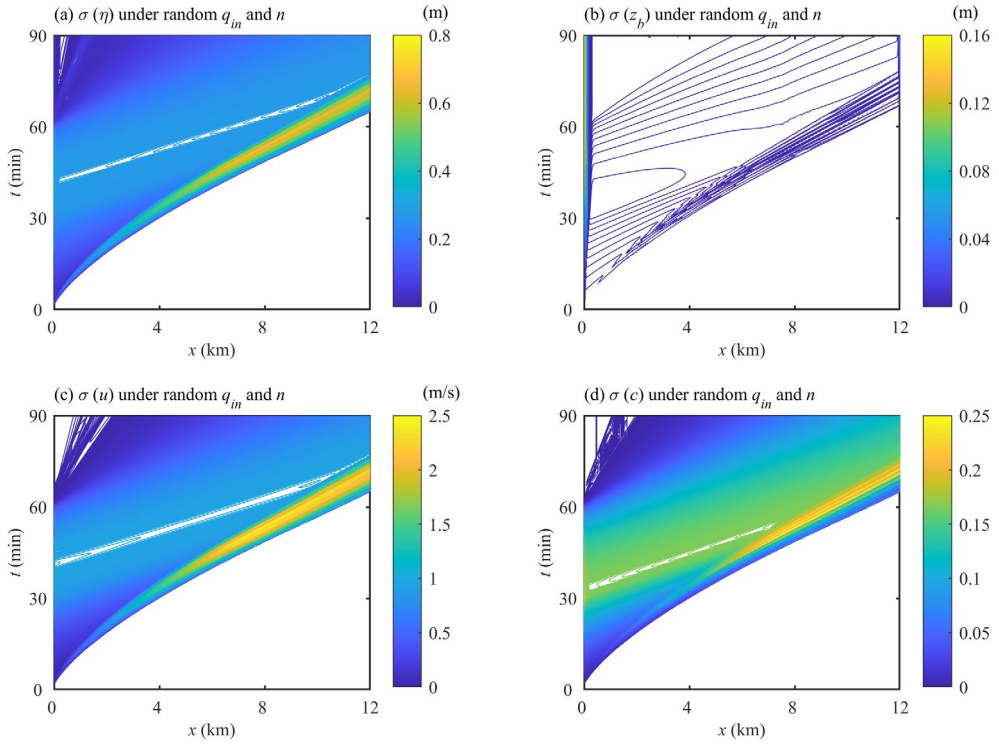

Fig. 11. Flash flood: spatial-temporal evolutions of standard deviations of (a) water surface, (b) bed elevation, (c) flow velocity and (d) sediment concentration for two joint uncertainties in inflow discharge $q_{in}(\xi_1)$ and Manning roughness parameter $n(\xi_2)$.

5. Conclusions

A new stochastic Galerkin SHSM model using Haar wavelet basis functions and an operator-splitting-based method is proposed for quantifying multiple joint uncertainties in modelling shallow water-sediment flows over erodible beds. With joint uncertainties introduced in initial and boundary conditions, a series of benchmark numerical tests are extended to probabilistic settings to verify the model for laboratory-scale flow-sediment-bed evolutions driven by a sudden dam break and by a landslide dam failure and large-scale rapid flow-sediment-bed evolution triggered by a flash flood. The model not only reasonably captures highly nonlinear flow-sediment-bed evolutions under multiple joint uncertainties,

but also yields possible realisation and standard deviation of the solutions.

The present work features an advance on modelling probabilistic shallow water-sediment flows over erodible beds. Extensions to two spatial dimensions and non-uniform sediments are essential for wider applications to natural flows. The excessive computational overheads due to “curse-of-dimensionality” when more uncertainty dimensions are considered can be alleviated by implementation of unstructured grids, parallel architecture and adaptive local-time-step techniques. These topics are reserved for future study.

Acknowledgements

This work was funded by the Natural Science Foundation of China under Grant No. 11802211 and the China Postdoctoral Science Foundation under Grant No. 2018M632917.

References

[1] W. Wu, Computational river dynamics, Taylor and Francis, London, UK, 2007.

[2] Z. Cao, G. Pender, S. Wallis and P. Carling, Computational dam-break hydraulics over erodible sediment bed, J. Hydraul. Eng. 130 (2004) 689–703. http://doi.org/10.1061/(ASCE)0733-9429(2004)130:7(689).

[3] J. Li, Z. Cao, G. Pender, Q. Liu, A double layer-averaged model for dam-break flows over mobile bed, J. Hydraul. Res. 51 (2013) 518–534. https://doi.org/10.1080/00221686.2013.812047.

[4] H. Qian, Z. Cao, G. Pender, H. Liu, P. Hu, Well-balanced numerical modeling of non-uniform sediment transport in alluvial rivers, Int. J. Sediment Res. 30 (2015) 117–130. http://doi.org/10.1016/j.ijsrc.2015.03.002.

[5] H. Qian, Z. Cao, H. Liu, G. Pender, Numerical modelling of alternate bar formation, development and sediment sorting in straight channels, Earth Surf. Proc. Land. 42 (2015) 555–574. https://doi.org/10.1002/esp.3988.

[6] C. Di Cristo, M. Greco, M. Iervolino, A. Leopardi, A. Vacca, Two-dimensional two-phase depth-integrated model for transients over mobile bed, J. Hydraul. Eng. 142 (2016) 04015043. http://doi.org/10.1061/(ASCE)HY.1943-7900.0001024.

[7] P. Hu, Y. Lei, J. Han, Z. Cao, H. Liu, Z. He, Computationally efficient modeling of hydro-sediment-morphodynamic processes using a hybrid local time step/global maximum time step, Adv. Water Resour. 127 (2019) 26-28. https://doi.org/10.1016/j.advwatres.2019.03.006.

[8] T. Takahashi, H. Nakagawa, T. Harada, Y. Yamashiki, Routing debris flows with particle segregation, J. Hydraul. Eng. 118 (1992) 1490-1507. https://doi.org/10.1061/(ASCE)0733-9429(1992)118:11(1490).

[9] E. D. Fernandez-Nieto, F. Bouchut, D. Bresch, M. C. Diaz, A. Mangeney, A new Savage-Hutter type model for submarine avalanches and generated tsunami, J. Comput. Phys. 24 (2008) 7720-7754. https://doi.org/10.1016/j.jcp.2008.04.039.

[10] A. Armanini, L. Fraccarollo, G. Rosatti, Two-dimensional simulation of debris flows in erodible channels, Comput. Geosci. 35 (2009) 993-1006.

https://doi.org/10.1016/j.cageo.2007.11.008.

[11] C. Adduce, G. Sciortino, S. Proietti, Gravity currents produced by lock exchanges: experiments and simulations with a two-layer shallow-water model with entrainment, J. Hydraul. Eng. 138 (2012) 111-121. https://doi.org/10.1061/(ASCE)HY.1943-7900.0000484.

[12] S. P. Pudasaini, A general two-phase debris flow model, J. Geophys. Res. 117 (2012) F03010. https://doi.org/10.1029/2011JF002186.

[13] Z. Cao, J. Li, G. Pender, Q. Liu, Whole-process modelling of reservoir turbidity currents by a double layer-averaged model, J. Hydraul. Eng. 141 (2015) 04014069. http://doi.org/10.1061/(ASCE)HY.1943-7900.0000951.

[14] J. Li, Z. Cao, K. Hu, G. Pender, Q. Liu, A depth-averaged two-phase model for debris flows over erodible beds, Earth Surf. Proc. Land. 43 (2018) 817-839. https://doi.org/10.1002/esp.4283.

[15] J. Li, Z. Cao, Y. Cui, A. G. L. Borthwick, Barrier lake formation due to landslide impacting a river: A numerical study using a double layer-averaged two-phase flow model, Appl. Math. Model. 80 (2020) 574-601. https://doi.org/10.1016/j.apm.2019.11.031

[16] J. Li, Z. Cao, A. G. L. Borthwick, Uncertainty quantification in shallow water-sediment flows: A stochastic Galerkin shallow water hydro-sediment-morphodynamic model, Appl. Math. Model. 99 (2021) 458-477. https://doi.org/10.1016/j.apm.2021.06.031.

[17] G. Di Baldassarre, G. Schumann, P. D. Bates, J. E. Freer, K. J. Beven, Flood-plain mapping: a critical discussion of deterministic and probabilistic approaches, Hydrol. Sci. J. 55 (2010) 364-376. https://doi.org/10.1080/02626661003683389.

[18] Y. Jung, V. Merwade, Uncertainty quantification in flood inundation mapping using generalized likelihood uncertainty estimate and sensitivity analysis, J. Hydrol. Eng. 17 (2011) 507-520. https://doi.org/10.1061/(ASCE)HE.1943-5584.0000476.

[19] J. Neal, C. Keef, P. D. Bates, K. Beven, D. Leedal, Probabilistic flood risk mapping including spatial dependence, Hydrol. Process. 27 (2013) 1349-1363. https://doi.org/10.1002/hyp.9572.

[20] D. Xiu, Fast numerical methods for stochastic computations: a review, Commun. Comput. Phys. 5 (2009) 242-272.

[21] D. Xiu, J. S. Hesthaven, High-order collocation methods for differential equations with random inputs, SIAM J. Sci. Comput. 27 (2005) 1118-1139. https://doi.org/10.1137/040615201.

[22] D. Xiu, Numerical methods for stochastic computations, Princeton University Press, Princeton, USA, 2010.

[23] D. Xiu, Efficient collocational approach for parametric uncertainty analysis, Commun. Comput. Phys., 2 (2007) 293-309.

[24] D. Xiu, J. Shen, Efficient stochastic Galerkin methods for random diffusion equations, J. Comput. Phys. 228 (2009) 266-281. https://doi.org/10.1016/j.jcp.2008.09.008.

[25] J. Hu, S. Jin, A stochastic Galerkin method for the Boltzmann equation with uncertainty, J. Comput. Phys. 315 (2016) 150-168. https://doi.org/10.1016/j.jcp.2016.03.047.

[26] R. Shu, J. Hu, S. Jin, A stochastic Galerkin method for the Boltzmann equation with multi-dimensional random inputs using sparse wavelet bases, Numer. Math-Theory Me., 10 (2017) 465-488. http://doi.org/10.4208/nmtma.2017.s12.

[27] S. Jin, R. Shu, A stochastic asymptotic-preserving scheme for a kinetic-fluid model for disperse two-phase flows with uncertainty, J. Comput. Phys., 335 (2017) 905-924. https://doi.org/10.1016/j.jcp.2017.01.059.

[28] L. Ge, K. F. Cheung, M. H. Kobayashi, Stochastic solution for uncertainty propagation in nonlinear shallow-water equations, J. Hydraul. Eng. 134 (2008) 1732–1743. https://doi.org/10.1061/(ASCE)0733-9429(2008)134:12(1732).

[29] J. Shaw, G. Kesserwani, Stochastic Galerkin finite volume shallow flow model: well-balanced treatment over uncertain topography, J. Hydraul. Eng. 146 (2020) 04020005. https://doi.org/10.1061/(ASCE)HY.1943-7900.0001705.

[30] J. Shaw, G. Kesserwani, P. Pettersson, Probabilistic Godunov-type hydrodynamic modelling under multiple uncertainties: robust wavelet-based formulations, Adv. Water Resour. 137 (2020) 103526. https://doi.org/10.1016/j.advwatres.2020.103526.

[31] R. Abgrall, S. Mishra, Uncertainty Quantification for Hyperbolic Systems of Conser-vation Laws, in: R. Abgrall, C. Shu (Eds.), Handbook of Numerical Analysis, Elsevier, 2017, vol. 18, pp. 507–544. https://doi.org/10.1016/bs.hna.2016.11.003.

[32] O.P.Le Maître, O. M. Knio, H. N. Najm, R. G. Ghanem, Uncertainty propagation using

Wiener–Haar expansions, J. Comput. Phys. 197 (2004) 28–57. https://doi.org/10.1016/j.jcp.2003.11.033.

[33] O.P.Le Maître, H. N. Najm, R. G. Ghanem, Multi-resolution analysis of Wiener-type uncertainty propagation schemes, J. Comput. Phys. 197 (2004) 502–531. https://doi.org/10.1016/j.jcp.2003.12.020.

[34] P. Pettersson, G. Iaccarino, J. Nordström, A stochastic Galerkin method for the Euler equations with Roe variable transformation, J. Comput. Phys. 257 (2014) 481–500. https://doi.org/10.1016/j.jcp.2013.10.011.

[35] P. Pettersson, H. A. Tchelepi, Stochastic Galerkin framework with locally reduced bases for nonlinear two-phase transport in heterogeneous formations, Comput. Methods Appl. Mech. Eng. 310 (2016) 367–387. https://doi.org/10.1016/j.cma.2016.07.013.

[36] A. Chertock, S. Jin, A. Kurganov, An operator splitting based stochastic Galerkin method for the one-dimensional compressible Euler equations with uncertainty. http://www.math.wisc.edu/~jin/research.html, 2015a (accessed 01 September 2021).

[37] A. Chertock, S. Jin, A. Kurganov, A well-balanced operator splitting based stochastic Galerkin method for the one-dimensional Saint-Venant system with uncertainty. http://www.math.wisc.edu/~jin/research.html, 2015b. (accessed 01 September 2021).

[38] B. Spinewine, Two-layer flow behaviour and the effects of granular dilatancy in dam-break induced sheetflow, Ph.D thesis, Universite´ Catholique de Louvain, Belgium, 2005.

[39] Z. Cao, Z. Yue, G. Pender, Landslide dam failure and flood hydraulics. Part I: experimental investigation, Nat. Hazards 59 (2011) 1003–1019. http://doi.org/10.1007/s11069-011-9814-8.

[40] I. Reid, J. B. Laronne, D. M. Powell, The Nahal Yatir bedload database: Sediment dynamics in a gravel-bed ephemeral stream, Earth Surf. Proc. Land. 20 (1995) 845–857. http://dx.doi.org/10.1002/esp.3290200910.

[41] D. Xiu, G. E. Karniadakis, The Wiener–Askey polynomial chaos for stochastic differential equations, SIAM J. Scientific Comput. 24 (2002) 619–644. https://doi.org/10.1137/S1064827501387826.

[42] G. Blatman, B. Sudret, Adaptive sparse polynomial chaos expansion based on least angle

regression, J. Comput. Phys. 230 (2011) 2345–2367. https://doi.org/10.1016/j.jcp.2010.12.021.

[43] E. F. Toro, Shock-capturing methods for free-surface shallow flows, John Wiley & Sons, Chichester, UK, 2001.

[44] Y. Zech, S. Soares-Fraz˜ao, B. Spinewine, N. Grelle, Dam-break induced sediment movement: Experimental approaches and numerical modelling, J. Hydraul. Res. 46 (2008) 176–190. https://doi.org/10.1080/00221686.2008.9521854.

[45] P. D. Bates, F. Pappenberger, R. J. Romanowicz, Uncertainty in Flood Inundation Modelling, in Applied uncertainty analysis for flood risk management, eds. K. J. Beven and J. Hall (Imperial College Press, London, 2014), pp. 232–269. https://doi.org/10.1142/9781848162716_0010.

[46] Z. Cao, P. Hu, G. Pender, Reconciled bedload sediment transport rates in ephemeral and perennial rivers, Earth Surf. Proc. Land. 35 (2010) 1655–1665. https://doi.org/10.1002/esp.2005.

https://chertock.wordpress.ncsu.edu/files/2018/05/CJK1.pdf

https://chertock.wordpress.ncsu.edu/files/2019/10/CJK2.pdf

List of figure captions

Fig.1. Idealized dam break over a fixed bed: model predictions of water surface and discharge at $t =$ 0.8 s using operator-splitting (solid lines) and non-splitting methods (dashed lines).

Fig. 2. Sudden dam break over an erodible bed: measurements (solid circles) from Spinewine [38] and probabilistic predictions of water surface and bed profiles (dashed lines) obtained for joint random Manning roughness parameter $n(\xi_1)$ and modification coefficient $\phi(\xi_2)$.

Fig. 3. Sudden dam-break: Spatial-temporal evolutions of standard deviations of (a) water surface, (b) bed elevation, (c) flow velocity, and (d) sediment concentration for joint random Manning's roughness parameter $n(\xi_1)$ and modification coefficient $\phi(\xi_2)$.

Fig. 4. Experimental setup for landslide dam failure [figure adapted from Cao et al. [39]].

Fig. 5. Landslide dam failure: measurements (open circles) for F-Case 11 from Cao et al. [39] and probabilistic predictions (dashed lines) of stage time histories at 4 gauge points along the flume for three joint uncertainties in inflow discharge $q_{in}(\xi_1)$, Manning roughness parameter $n(\xi_2)$, and modification coefficient $\phi(\xi_3)$.

Fig. 6. Landslide dam failure: measured water surface (open circles) for F-Case 11 from Cao et al. [39] and probabilistic predictions of water surface, and bed profiles (dashed lines) along a channel for three joint uncertainties in inflow discharge $q_{in}(\xi_1)$, Manning roughness parameter $n(\xi_2)$, and modification coefficient $\phi(\xi_3)$.

Fig. 7. Landslide dam failure: spatial-temporal evolutions of standard deviations of (a) water surface, (b) bed elevation, (c) flow velocity and (d) sediment concentration for three joint uncertainties in inflow discharge $q_{in}(\xi_1)$, Manning roughness parameter $n(\xi_2)$, and modification coefficient $\phi(\xi_3)$.

Fig. 8. Flash flood: measurements (open circles) and probabilistic predictions (dashed lines) of sediment transport rate against shields parameter at selected cross-sections for two joint uncertainties in inflow discharge $q_{in}(\xi_1)$ and Manning roughness parameter $n(\xi_2)$.

Fig. 9. Flash flood: probabilistic predictions of (a1-a4) discharge (black dashed lines) and (b1-b4) sediment transport rate (blue dashed lines) time histories at four cross-sections for two joint uncertainties in inflow discharge $q_{in}(\xi_1)$ and Manning roughness parameter $n(\xi_2)$.

Fig. 10. Flash flood: probabilistic predictions of stage (black dashed lines) and bed elevation (blue dashed lines) time histories at four cross-sections for two joint uncertainties in inflow discharge $q_{in}(\xi_1)$ and Manning roughness parameter $n(\xi_2)$.

Fig. 11. Flash flood: spatial-temporal evolutions of standard deviations of (a) water surface, (b) bed elevation, (c) flow velocity and (d) sediment concentration for two joint uncertainties in inflow discharge $q_{in}(\xi_1)$ and Manning roughness parameter $n(\xi_2)$.

List of table captions